Characterization of the nature and morphology of coarse precipitation in various oxide dispersion strengthened steels

Gabriel Spartacus, Joël Malaplate, Denis Menut, Caroline Toffolon-Masclet, Denis Sornin, Frédéric de Geuser, Raphaëlle Guillou, Amélie Gangloff, Arnaud Lequien, Stéphane Urvoy, et al.

Characterization of the nature and morphology of coarse precipitation in various oxide dispersion strengthened steels

Gabriel Spartacus [a], Joël Malaplate [a,*], Denis Menut [c], Caroline Toffolon-Masclet [a], Denis Sornin [a], Frédéric De Geuser [b], Raphaëlle Guillou [a], Amélie Gangloff [a], Arnaud Lequien [a], Stéphane Urvoy [a], Alexis Deschamps [b]

[a] Université Paris-Saclay, CEA, Service de Recherches Métallurgiques Appliquées, 91191 Gif-sur-Yvette Cedex, France

[b] SIMAP, Grenoble INP – CNRS – UJF, 1130 rue de la Piscine BP 75, 38402 Saint Martin d'Hères Cedex, France.

[c] Synchrotron SOLEIL, L'Orme des Merisiers, Saint Aubin BP48, 91192 Gif-sur-Yvette Cedex, France

[*] Corresponding author: joel.malaplate@cea.fr

Keywords: Oxide Dispersion Strengthened (ODS) steel, Precipitation, Carbides, Nitrides, Oxides, Transmission Kikuchi Diffraction (TKD), X-ray Diffraction (XRD)

Highlights

- Cr-carbides, Ti(C,N) and Ti-O were found in Oxide Dispersion Strengthened steels.
- Fe-14Cr grades display both $M_{23}C_6$ and M_7C_3 where Fe-9Cr grades display only $M_{23}C_6$.
- Cr-carbide are elongated in extruded alloys and Ti(C,N) are globular.
- Ti-O are mostly located at the prior particles boundaries.
- At ~700°C, $M_7C_3 \rightarrow M_{23}C_6$ transformation is likely and not suitable for industrial use.

Graphical abstract

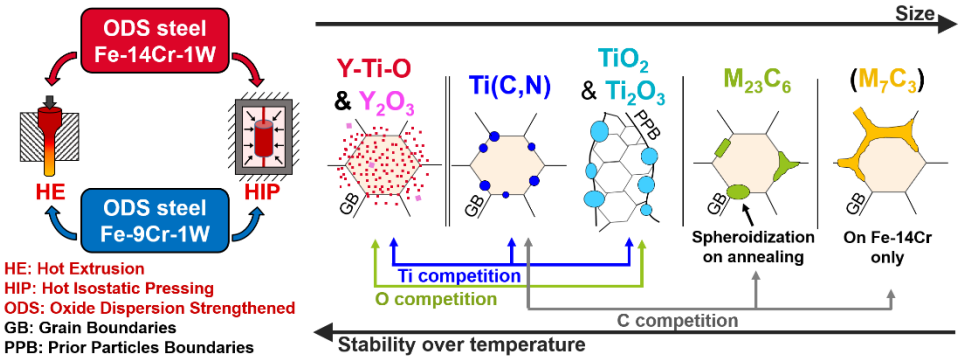

Abstract

Oxide Dispersion Strengthened (ODS) steels are candidate materials for both fission and fusion nuclear reactors. In this study, the microstructure of ferritic (Fe-14Cr-1W) and ferritic / martensitic (Fe-9Cr-1W) ODS steels has been characterized after two different processing routes: Hot Extrusion (HE) and Hot Isostatic Pressing (HIP). Transmission Kikuchi Diffraction (TKD) revealed the presence of Ti-rich precipitates on every specimen. They are identified by X-ray Diffraction (XRD) as Ti(C,N) and Ti-O (Ti_2O_3 or TiO_2). Intergranular M_7C_3 and $M_{23}C_6$ have been observed on most Fe-14Cr ODS steels except one, where no Cr-carbides have been found. In Fe-9Cr ODS, intergranular Cr-rich $M_{23}C_6$ carbides have been found. This absence of M_7C_3 on Fe-9Cr ODS is possibly linked to the matrix phase transformation, not occurring in the Fe-14Cr ODS. Cr-carbides display highly elongated shapes for the Fe-14Cr HE specimens that could be detrimental to the mechanical behavior of the material.

1. Introduction

Oxide Dispersion Strengthened (ODS) steels are among the most promising candidates for an application as cladding materials in generation IV nuclear power plants [1], as well as first wall and breeder blanket structural materials in fusion nuclear power plants [2]. Fe-Cr ODS steels strengthened by Y-Ti-O nano-oxides are processed by powder metallurgy involving a mechanical alloying step where an atomized Fe-Cr steel powder is mixed together with an oxide powder. This milling step, so called Mechanical Alloying (MA) is followed by a consolidation step of Hot Extrusion (HE) or Hot Isostatic Pressing (HIP) both performed at high temperature. This process leads to a dense material and the formation of distinct precipitates:

- Y-Ti-O nano-oxides deliberately included, with a typical number density of 10^{23} to 10^{24} precipitates per m^{-3} and diameter of a few nanometers [3]–[6];
- coarse oxides, generally titanium oxides, mainly found as globular particles with size varying from a few tens to hundreds of nm [5]–[7];
- carbides precipitation, in many cases composed of intergranular $M_{23}C_6$. This precipitation is induced by the C impurities present into the atomized steel powder, increased by the subsequent fabrication process, especially the milling step [8], [9]. This precipitation is detrimental to the mechanical properties of the ODS alloys [6], [10]–[12], especially by decreasing their creep resistance [13].

The composition in Cr of the atomized steel powder will define if the alloy is purely ferritic (Cr content >12wt%) or ferritic / martensitic (Cr content <12wt%). Purely ferritic steels exhibit a good corrosion resistance but are more complex to process and display anisotropic behavior. The processing of ferritic / martensitic grades is easier due to the phase transformation, which induces a structural recovery. Nevertheless, the corrosion resistance of these grades is lower,

which is prejudicial to the fuel reprocessing process involving the immersion of the cladding into a nitric acid solution. Moreover, the phase transformation from ferrite (α) to austenite (γ) could be detrimental to their application above 850°C.

The mechanical properties of ODS steels at high temperature originate mainly from the dispersion of nano-oxides, which act as pinning points for both grain boundaries (GB) and dislocations. These nano-oxides are very stable until 1200°C, which is much higher than the maximum service temperature potentially encountered in fast neutron reactors (i.e. 650°C) [14], [15]. Thanks to these properties, the dispersion of nano-oxides proves to be a very efficient way to prevent thermal creep by significantly increasing the creep rupture time. Therefore, previous studies on ODS steels have been mainly focused on the nanoscale precipitation. Nowadays, the outstanding properties of the nano-oxide dispersion in terms of number density, mean size and thermal stability make any improvement challenging without a disruptive innovation. However, an optimization of the coarse precipitation can be achieved using thermal or thermomechanical treatments. Indeed, Klimiankou *et al.* demonstrated the possibility to transform the morphology of chromium carbides (Cr-carbides) in EUROFER-97 ODS steel by different thermomechanical treatments [16]. Klimiankou *et al.* linked this change in Cr-carbides morphology to an improvement in tensile ductility as well as a decrease of the ductile to brittle transition temperature. Later, Zhao *et al.* succeeded to transform $M_{23}C_6$ type carbides into finer and globular TiC carbides in a Fe-14Cr-2W grade ODS by applying a thermal treatment, once again improving the tensile properties of the alloy [17]. Thus, mastering the coarse precipitation seems to be a promising way to improve the control on the complex microstructure of ODS steels and potentially enhance their mechanical behavior.

Prior to a potential optimization, a careful characterization of the coarse precipitates population in various ODS grades obtained by different processing routes is needed. For this purpose, we performed systematic multi-scale observations using Electron Probe Micro Analysis (EPMA), Transmission Kikuchi Diffraction (TKD) and X-Ray Diffraction (XRD) to identify the nature and morphology of the coarse precipitation on several Fe-14Cr-1W and Fe-9Cr-1W ODS steels processed by means of HE or HIP.

2. Materials and methods

Two grades of ODS steels with two different chromium contents have been investigated in this study: a Fe-14Cr-1W purely ferritic grade and a Fe-9Cr-1W ferritic / martensitic grade, which exhibits a phase transformation around 850°C from ferrite (α) to austenite (γ) [18]–[20]. Two processing batches of HE and one of HIP were performed for the 14Cr ODS grades (named respectively HE-14Cr, HE-14Cr-PMill and HIP-14Cr) and for the 9Cr ODS grades (named respectively HE-9Cr, HE-9Cr-PMill and HIP-9Cr).

Except for HE-14Cr-PMill and HE-9Cr-PMill all the alloys were Mechanically Alloyed (MA) at the CEA using attrition milling for 10 hours from an atomized Fe-Cr steel, together with Y_2O_3 and TiH_2 powders under high purity argon (99.9999%Ar). HIP and HE were then prepared from the same powders, milled separately following the same process. HE-14Cr-PMill and HE-9Cr-PMill were mechanically alloyed by PLANSEE (PMill then states for PLANSEE Milling) following slightly different milling parameters with a similar milling time.

Irrespective of their milling, as-MA powders were outgassed at temperatures varying from 400 to 500°C for 4 to 8 hours under vacuum at 10^{-6} mbar and sealed into low carbon steel cans. Before HE processing, the filled cans were placed in a furnace at 1100°C, the milled powder following then a heating ramp at ~40°C/min until 1100°C followed by ~1h isothermal. Then, the heated cans of diameter approximatively 75 mm were hot extruded under a load of 575 tons inducing a downstream motion of 25mm/s of the steel cans into a circular die producing a section reduction of around 12 times. HE were then followed by air-cooling of the extruded bar. Hot Isostatic Pressing (HIP) involved a heating ramp of the steel can at around 4°C/min until 1100°C with a simultaneous increase of the pressure up to 1.9×10^{8} Pa followed by 2 hours isothermal and a cooling at around -4°C/min. For the elaboration of HE-14Cr and HIP-14Cr the base powders (atomized Fe-Cr, Y_2O_3 and TiH_2) were used but coming from two different batches of milling, as well as for HE-14Cr and HIP-9Cr.

The different processes and chemical composition of all the specimens used in this study are reported in

Tab. **1**. Additionally to these elements, a composition of around ~0.3Mn, ~0.3Si and ~0.2Ni in weight percent are present in every ODS grades, as well as ~100 to 500 ppm of Al as impurities coming from the MA process.

Tab. 1. Chemical compositions and processing routes of studied ODS steels expressed in weight percent.

Name	Process	Fe	Cr	W	C	N	Ti*	Y_2O_3*
HE-14Cr	HE + 1050°C 1h	Bal.	14.2	0.95	0.045	0.071	0.3	0.3
HE-14Cr-PMill	HE + 1050°C 1h	Bal.	~14	~1	<0.05	<0.1	0.3	0.25
HIP-14Cr	HIP	Bal.	14.5	0.93	0.028	0.039	0.3	0.3
HE-9Cr	HE + 1050°C 1h	Bal.	~9	~1	~0.1	<0.1	0.3	0.3
HE-9Cr-PMill	HE	Bal.	~9	~1	~0.1	<0.1	0.3	0.25
HIP-9Cr	HIP	Bal.	~9	~1	~0.1	<0.1	0.3	0.3

* Amount of strengthening media added to the mechanical alloying step

After HE, three specimens followed an additional heat treatment at 1050°C for 1 hour in order to release the internal stresses induced by the severe deformation of the extrusion process (HE-14Cr, HE-14Cr-PMill and HE-9Cr).

Scanning Electron Microscopy (SEM) were performed on a JEOL 7001-FLV instrument using Energy Dispersive Spectroscopy (EDS) coupled with Transmission Kikuchi Diffraction (TKD) methods performed on a Bruker QUANTAX system (Esprit software). The operating voltage was set to 30 kV with a working distance of about 5 mm achieving a spatial resolution of around 20 nm. For the phase identification of TKD measurements PDF4+ database was used. For our study, the distinction between TKD identification of Ti_2O_3 and TiO_2 phases was not considered as relevant enough. Therefore, the two phases have been treated as a single one named "Ti-O". M_6C and $M_{23}C_6$ carbides both have a similar face centered cubic structure with a lattice parameters of 11 Å and 10.65 Å respectively [21], [22]. Therefore, these phases could not be distinguished by single TKD indexing but could be easily distinguished using comparison of TKD and EDS results. Indeed, $M_{23}C_6$ is generally found to be rich in Cr and Fe with a little W and M_6C is found to be rich in Fe and W with a little Cr and a stoichiometry close to Fe_3W_3C [23]. Ferrite Fe-α, Cr_7C_3 orthorhombic and Ti(C,N) phases were successfully distinguished and identified. TKD orientation maps displayed in this study only show the ferrite phase orientation with the corresponding orientation to colors given on Fig. 2c. Specimens were mechanically grinded into thin foils of 100 µm in thickness and electro-polished using an etchant solution of 10% perchloric acid ($HClO_4$) with 90% ethanol (C_2H_6O) at -10°C using a Struers TenuPol device. On three EDS map (Fig. 2a', Fig. 9a and Fig. 11a) parallel lines with a slight contrast appear. Those lines should not be taken into account, as they are present on all elemental maps

and had been attributed to a detector deficiency. TKD measurements were performed on at least three separated areas of each specimen, generally taken on the same thin foil.

Electron Probe Micro Analyses (EPMA) were performed, using a SX 100 CAMECA device to probe the presence of C, O, Ti, Cr, Mn, Fe, Y, and W. The acceleration voltage was set to 15 kV, with a step size of 1 µm or 0.5 µm depending on the magnification used.

Approximately 28.5 g of each HE-14Cr-PMill and HE-9Cr-PMill followed an electrolytic selective dissolution process in a solution of methanol and chloridric (HCl) acid at a dissolution rate of around 1.5 $g.h^{-1}$. Subsequently, the solution was filtrated using a Buchner membrane with a porosity of 220 nm. Obtained powder was then dried at 60°C for 24 hours. This matrix dissolution allowed to enhance the intensity of secondary phases over the suppressed ferrite. Moreover, it can also provide an approximation of the massic fraction of precipitates by weighting before and after dissolution. However, due to the size of the filter pores, Y-Ti-O nano-precipitates may not be gathered in totality. Then, reflection X-Ray Diffraction (XRD) measurements were performed on a laboratory D8 diffractometer using a Cu anode at the K-α edge (wavelength of 1.54 Å). Powders were placed on a rotating specimen holder (at 15 rotations per second), a 3 seconds counting time was applied with an angular step of 0.0187° on a 2θ angle ranging from 13° to 140°.

On the HE-14Cr, HIP-14Cr and HE-9Cr materials, transmission XRD measurements were performed at the MARS beamline of the SOLEIL synchrotron (Saint Aubin, France) [24]. A bi-dimensional imaging-plate detector MAR345 (marXpert GmbH) with an incoming energy of 12.51 keV and a sample to detector distance of 258 mm was used. Ten 2D images per sample were acquired with a counting time ranging from 600 to 3600 sec, averaged and azimuthally integrated.

On both synchrotron and laboratory X-ray sources, diffraction patterns were background subtracted and corrected using a LaB_6 sample (NIST SRM 660b) as a standard. Intensity has been normalized by the most intense pic. The Le Bail Full Pattern Matching Method was performed with the MAUD v2.91 software [25], [26] for fitting lattice parameters of phases assuming an isotropic size (Gaussian contribution) – strain (Lorentzian contribution) model considering a Pseudo-Voigt line profile-function with axial divergence [27], [28].

In order to predict the equilibrium phases, thermodynamic calculations were performed using ThermoCalc software with the database TCFe_8 [29]. For each grade (Fe-14Cr and Fe-9Cr) the phase diagram was simulated, considering an amount of 1wt% of W, 0.3wt% of Ti and 0.07wt% of N. One simulation was made with an additional amount of 0.2wt% O that represents a reasonable maximum value of the oxygen added by the addition of 0.3wt% of Y_2O_3 and by the processing steps. Some simulations were performed by suspending the precipitation of $M_{23}C_6$ in order to evaluate the evolution of the M_7C_3 stability domain.

3. Results

The results are separated into two sections: purely ferritic ODS steel containing 14wt% of Cr and ferritic / martensitic steel with 9wt% of Cr.

3.1. Fe-14Cr-1W purely ferritic ODS steels

EPMA results on purely ferritic Fe-14Cr ODS steels show a homogeneous repartition of Cr, W and Y at large scale, exempt of coarse precipitates with size larger than 5 µm. However, Ti and O tend to segregate at the interphases of domains with size and morphologies relevant to prior powder particles (Fig. 1). Similar observations were also reported for various ODS steels processed by HE [30], by hot uniaxial compression [31] and by spark plasma sintering [32].

All Fe-14Cr microstructures exhibit a wide range of grain sizes with a strong dependence on the fabrication process. As a result of the severe deformation, HE alloys present columnar shaped grains, with a possible <110> texture along the extrusion direction (Fig. 2 and Fig. 3). HIP processed grades present equiaxed grains with an apparently random texture (Fig. 4). As the number of grains counted in high magnified TKD measurement is limited, our observations do not allow to be decisive. The measured average grain size was determined considering an elliptical shape in the plane parallel to the extrusion direction for the HE-14Cr-PMill grade and determined to be 2.6x0.5 µm. It should be noted that whereas the minor axis of the elongated grain size shows a relatively low dispersion, the major axis exhibits a significant dispersion with standard deviation of the measurements as high as 200% of the mean value. This value was calculated over several EBSD maps offering wide field of view (maps not presented here). According to Dadé *et al.* who made a similar analysis, the grain size of the HE-14Cr is 1.2x0.4 µm and the HIP-14Cr grade shows an average grain size of 6.5 µm [33].

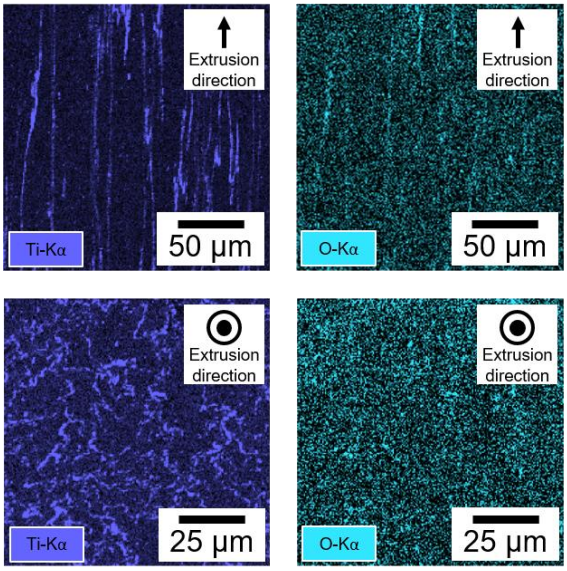

Fig. 1. EPMA maps of the HE-14Cr-PMill specimen at Ti and O K-α wavelengths showing a cross-section parallel and perpendicular to the extrusion direction.

On each Fe-14Cr alloys, regardless to their fabrication route, titanium rich particles were found on the EDS map (Fig. 2a, a', Fig. 3a, a' and Fig. 4a). Due to their very small size, Ti-rich precipitates identification using the TKD technique was challenging and rarely successful. Indeed, TKD identification is very sensitive to Kikuchi patterns overlapping originating from the successive scattering of superposed phases along the specimen's thickness. Such overlapping considerably lowers the pattern clarity and thus the ability to identify the phase. Nevertheless, EDS maps revealed that Ti-rich particles exhibit globular shapes. These Ti-rich particles appear to be intergranular by considering the superposition of EDS map (resolving the Ti-rich precipitates) to TKD map (displaying the GBs). This superposition should be considered with caution, keeping in mind the difference of probed volume by EDS and TKD. Indeed, EDS probes the element presence in the whole thickness of the TEM foil, with a more intense signal at the top surface while TKD is more sensitive to the GBs at the bottom surface.

The phase mapping on the HE-14Cr-PMill specimen succeeded to identify few Ti(C,N) small precipitates of diameter about 100 nm (Fig. 2b and b'). On this figure, few pixels were also identified as Ti-oxides but this identification was not considered as relevant regarding the size of the domains indexed. On the HE-14Cr and HIP-14Cr grades, the Cr_7C_3 structure was identified, and matching with area enriched in Cr in EDS mapping. This carbide was absent of the HE-14Cr-PMill material (Fig. 2b, b', Fig. 3b, b' and Fig. 4b). These carbides are likely to contain Fe and Cr in agreement with our Thermocalc simulations (see below), and thus will be labeled M_7C_3 in the following. M_7C_3 carbides are always intergranular with a morphology that follows the shapes of GBs. In particular, the HE-14Cr specimen (Fig. 3) clearly displays elongated Cr-carbides in the extrusion direction following the path of GBs.

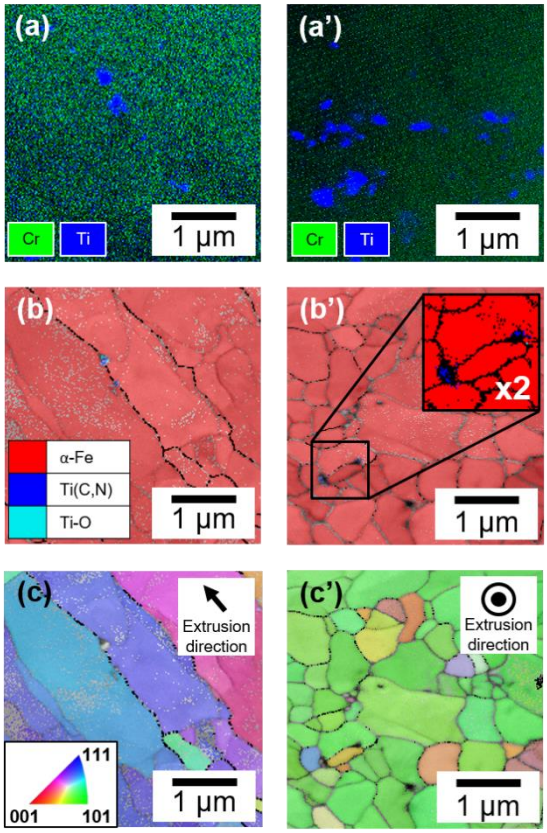

Fig. 2. HE-14Cr-PMill specimen showing EDS map for Cr and Ti (a), TKD phase map showing the presence of Ti carbides (b), TKD orientation map (c), parallel to the HE direction, and respectively for the perpendicular direction (a'), (b'), (c').

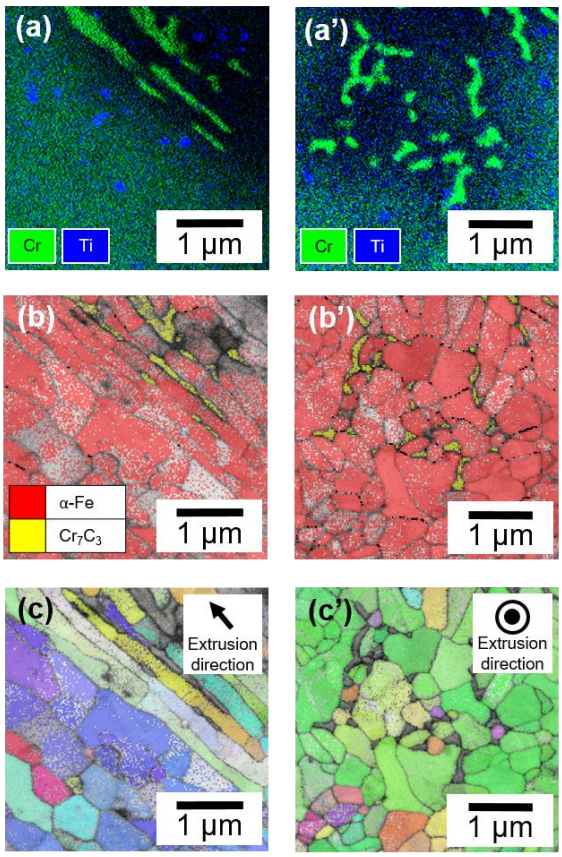

Fig. 3. HE-14Cr specimen showing EDS Cr-Ti map (a), TKD phase identification displaying M_7C_3 (b), TKD orientation map (c), parallel to the HE direction, and respectively for the perpendicular direction (a'), (b'), (c').

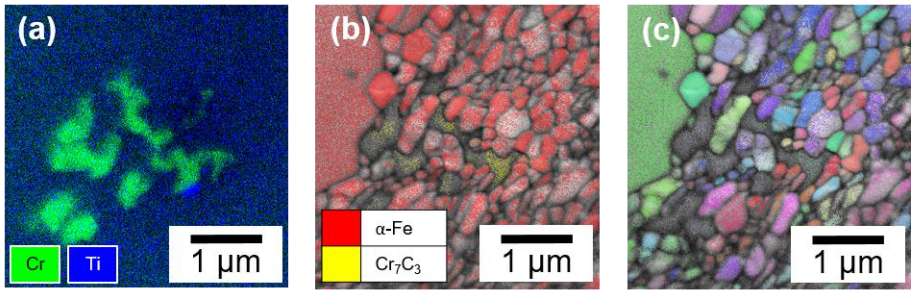

Fig. 4. HIP-14Cr specimen showing EDS Cr-Ti map (a), TKD phase map with intergranular M_7C_3 identification (b), and TKD orientation map (c).

XRD measurements have been performed on the selective dissolution of HE-14Cr-PMill specimen using laboratory source (Fig. 5), and on the bulk material for the HE-14Cr and HIP-14Cr materials using synchrotron source (Fig. 6).

On the HE-14Cr-PMill the Ti(C,N) phase was clearly identified and exhibits a high relative volume fraction, confirming the TKD measurements with a higher statistical reliability. The

cell parameter was refined to 4.256 Å which is consistent with that of the $Ti(C_x,N_{1-x})$ with $x \approx 0$ phase (2.245 Å) [34]. Moreover, the peak intensity ratio had been found consistent with a high content of N over C, refined as approximately $Ti(C_{0.05},N_{0.95})$. Ti_2O_3 and $Y_2Ti_2O_7$ phases were also identified with a lower relative volume fraction. The total mass fraction of precipitates in the HE-14Cr-PMill was estimated at ~1% thanks to the selective dissolution weighted mass ratio.

In the HE-14Cr and HIP-14Cr materials, Ti(C,N) with both M_7C_3 and $M_{23}C_6$ carbides were found, demonstrating the presence of $M_{23}C_6$ and Ti(C,N) in these grades in addition to the M_7C_3 observed by TKD. In these specimens, the N to C ratio could not be refined with a good reliability due to the difficulty to fit the overlapping and very intense Fe peak with a high accuracy. However, the Ti(C,N) cell parameter was once again in good agreement with N rich precipitate phase (**Tab. 2**). As for the presence of oxides, contrary to HE-14Cr-PMill sample, only TiO_2 were found in the bulk sample diffraction patterns, nevertheless, the low volume fraction of Ti-oxides do not allow to exclude the presence of Ti_2O_3 in these grades as well.

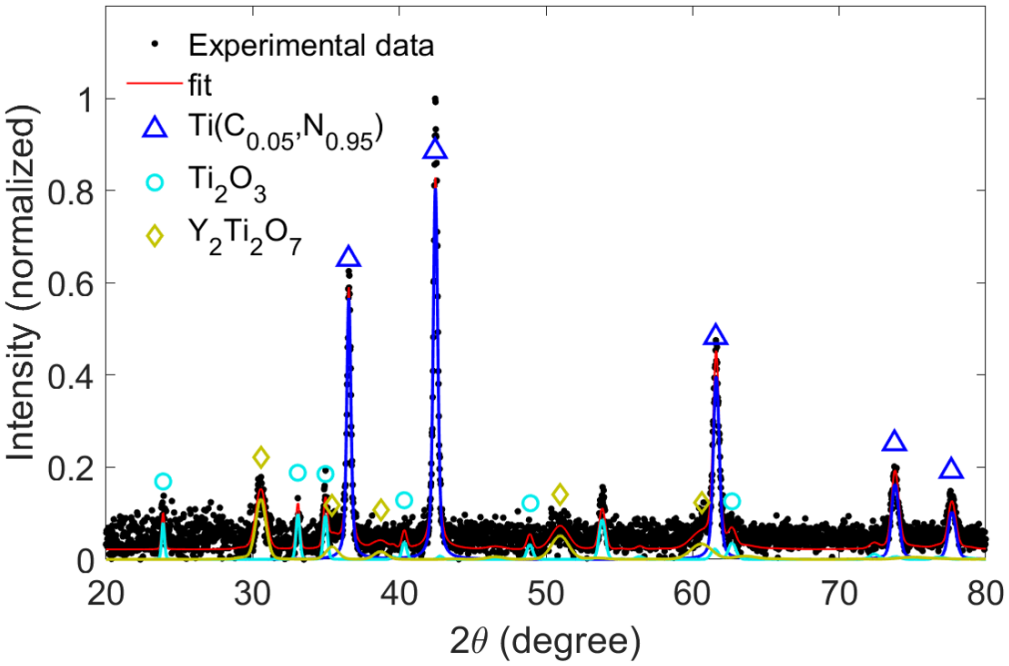

Fig. 5. Laboratory XRD spectrum of the selective dissolution of HE-14Cr-PMill specimen showing $Ti(C_{0.05},N_{0.95})$, Ti_2O_3 and $Y_2Ti_2O_7$ phase identification.

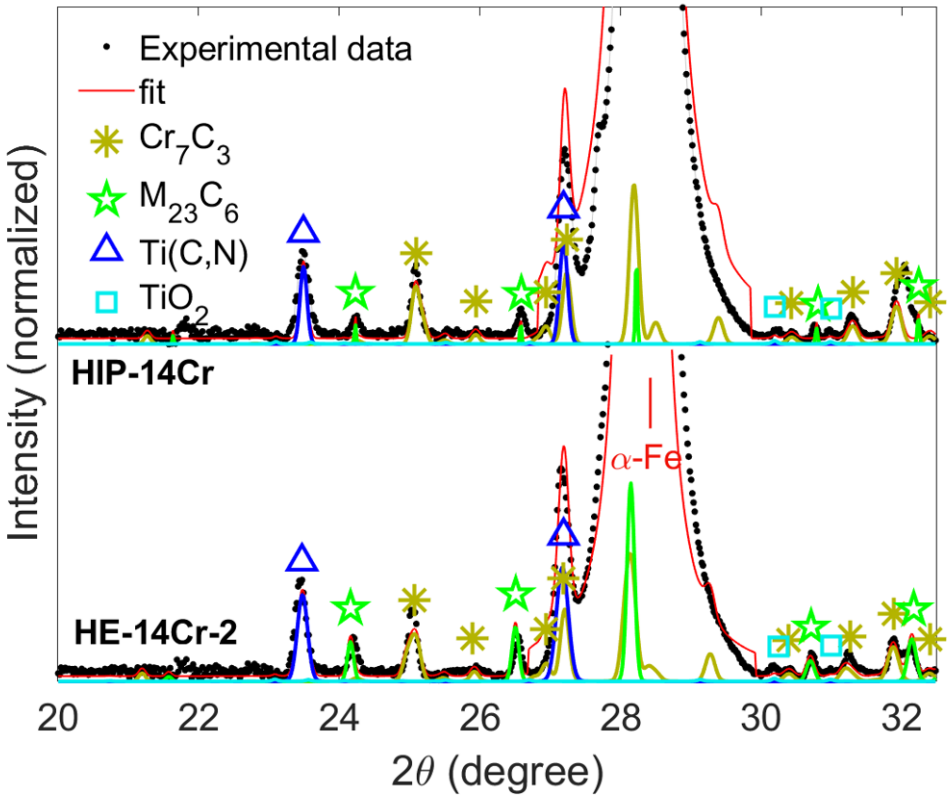

Fig. 6. Synchrotron XRD spectrum of the HE-14Cr and HIP-14Cr specimens showing Cr_7C_3 structure, $Cr_{23}C_6$ structure, Ti(C,N), TiO_2 phase identification.

Tab. 2. Fe-14Cr-1W ODS phases parameters after refinements with estimated errors, reference phases used are completed with space groups and corresponding references.

Phase name	Specimen	Volume fraction	Refined cell parameters (Å)	Reference Phase
HE-14Cr	M_7C_3	0.29 %	a = 4.493 (±0.006) b = 7.008 (±0.015) c = 12.068 (±0.024)	Cr_7C_3 Pnma [35]
	$M_{23}C_6$	0.10 %	a = 10.585 (±0.005)	$Cr_{23}C_6$ Fm-3m [21]
	Ti(C,N)	0.28 %	a = 4.219 (±0.004)	Ti(C,N) Fm-3m [34]
	TiO_2	0.05 %	a = 5.141 (±0.047) b = 9.210 (±0.355) c = 5.504 (±0.175)	TiO_2 Pbca [36]
	α-Fe	99.28%	a=2.865 (neglectable)	α-Fe Im-3m [37]
HE-14Cr-PMill	$Ti(C_{0.05},N_{0.95})$	66.0 %	a = 4.256 (±0.0003)	Ti(C,N) Fm-3m [34]
	Ti_2O_3	17.9 %	a = 5.132 (±0.002) b = 13.652 (±0.008)	Ti_2O_3 R-3cH [38]
	$Y_2Ti_2O_7$	16.0 %*	a = 10.133 (±0.006)	$Y_2Ti_2O_7$ Fd-3m [39]
HIP-14Cr	M_7C_3	0.26 %	a = 4.488 (±0.006) b = 6.987 (±0.014) c = 12.014 (±0.020)	Cr_7C_3 Pnma [35]
	$M_{23}C_6$	0.08 %	a = 10.556 (±0.004)	$Cr_{23}C_6$ Fm-3m [21]
	Ti(C,N)	0.18 %	a = 4.214	Ti(C,N)

		(±0.003)	Fm-3m [34]
TiO_2	0.05 %	a = 9.209 (±0.244) b = 5.496 (±0.113) c = 5.136 (±0.056)	TiO_2 Pbca [36]
α-Fe	99.51%	a = 2.861 (neglectable)	α-Fe Im-3m [37]

* Relative volume fraction of $Y_2Ti_2O_7$ is probably underestimated as the smaller precipitates were possibly not gathered by the filter.

As expressed in section 2, phase diagrams have been calculated using the Thermocalc software. Results have been computed for a Fe-14Cr-1W-0.3Ti-0.07N steel with and without precipitation of $M_{23}C_6$ and on a Fe-14Cr-1W-0.3Ti-0.07N-0.2O without $M_{23}C_6$ precipitation (Fig. 7). These diagrams indicate the presence of $Ti(C_x,N_{1-x})$ precipitates more enriched in N than in C for all temperatures and all carbon contents. The x value in $Ti(C_x,N_{1-x})$ could then achieve 0.8 on the two first diagrams (without O) and 0.9 for the last diagram with 0.2wt% of O. By suspending the $M_{23}C_6$ precipitation, the stability domain of M_7C_3 extend to much lower C content, previously occupied by $M_{23}C_6$. The M_7C_3 stability domain extend even more to lower carbon content when O is introduced. Finally, our observations showing the absence of M_6C precipitates is coherent with Thermocalc diagrams where this phase is only stable for high amount of C (around 1wt%) far above the 0.1wt% expected, in the simulation containing oxygen. On the diagram containing oxygen $(Ti,Cr)_2O_3$ is the only Ti-O phase predicted, irrespective of the C content and until high temperature > 1100°C.

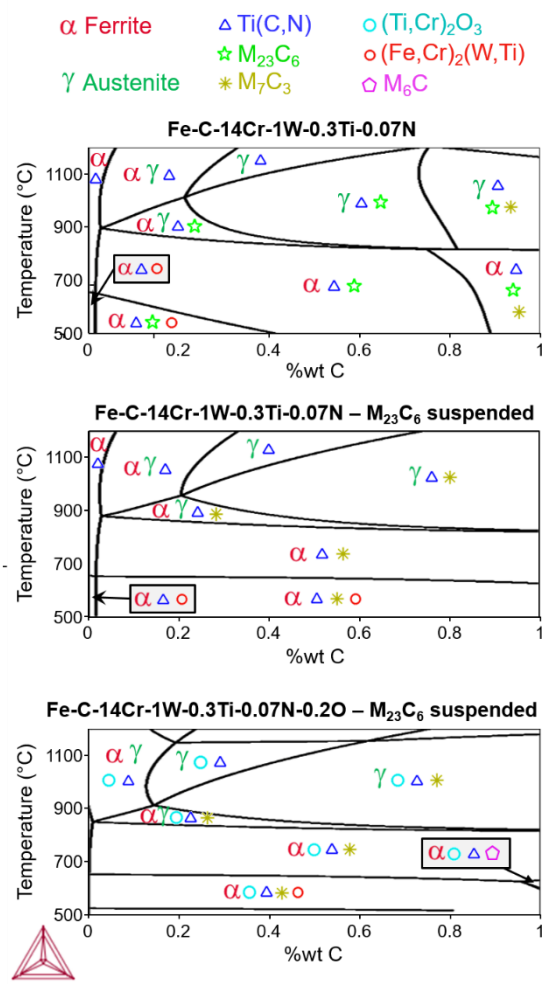

Fig. 7. Simulated phase diagrams of Fe-14Cr-1W-0.3Ti-0.07N(-0.2O) steels computed by Thermocalc software displaying several scenarios with and without $M_{23}C_6$ precipitation.

3.2. Fe-9Cr-1W ferritic / martensitic ODS steels

In the 9Cr grades, EPMA analyses do not display a significant Ti segregation at Prior Particles Boundaries (PPB) like on the 14Cr grades. However, precipitates enriched in Cr, C, possibly W and depleted in Fe can be identified, even if their sizes were near the spatial resolution limit of the measurement (Fig. 8). In addition, Ti and O rich spots appear to be correlated (and independent of the Cr and C). However, their even smaller size makes any conclusion at this scale challenging.

Each of the observed Fe-9Cr ferritic / martensitic ODS steels appears to be without marked texture even when processed by HE but keeps a wide range of grain sizes. However, as our TKD observations allow only the distinction of few grains we could not exclude the presence of a slight texture. The measured average grain size is 1.6 µm for the HE-9Cr-PMill material based on a wide view given by EBSD mapping (not presented here).

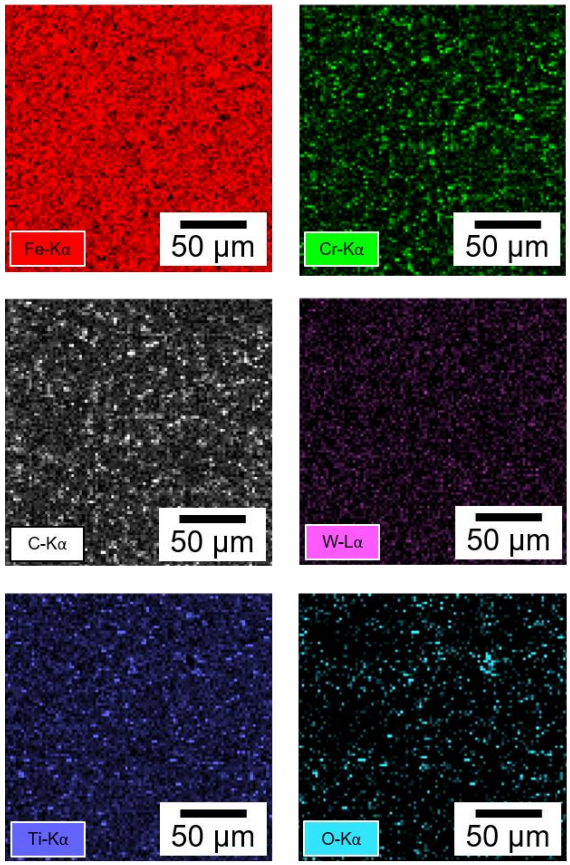

Fig. 8. EPMA maps of the HE-9Cr-PMill specimen.

EDS maps show Ti-rich globular precipitates, probably intergranular, similar to those observed on the 14Cr ODS steels (Fig. 9a, Fig. 10a and Fig. 11a). On the HE-9Cr specimen, one Ti-O precipitate was identified with an approximate diameter of 0.3 µm (Fig. 10c). However, the majority of the Ti-rich precipitates could not be identified using TKD maps. The Cr-carbides identification achieved a significantly higher success rate and demonstrates the presence of Cr-rich $M_{23}C_6$ type carbides in each of the 9Cr alloys (Fig. 9c, Fig. 10c and Fig. 11c). The $M_{23}C_6$ carbides, systematically intergranular, exhibit a shape following the GB in HE-9Cr-PMill and HIP-9Cr alloys and rather globular shapes in the HE-9Cr specimen. In addition, a W enrichment was found in many $M_{23}C_6$ precipitates which was absent of the previously observed M_7C_3 carbides embedded in the Fe-14Cr alloys.

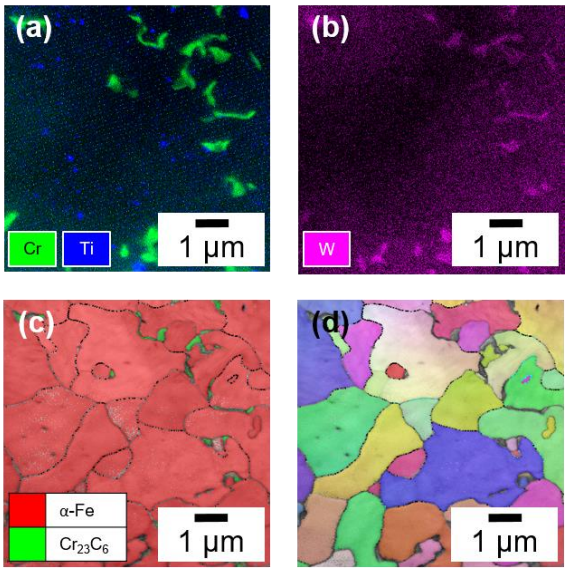

Fig. 9. HE-9Cr-PMill specimen showing EDS Cr-Ti map (a) and W map (b), TKD phase map with grain boundaries shaped $Cr_{23}C_6$ structure identification (c), and TKD orientation map (d).

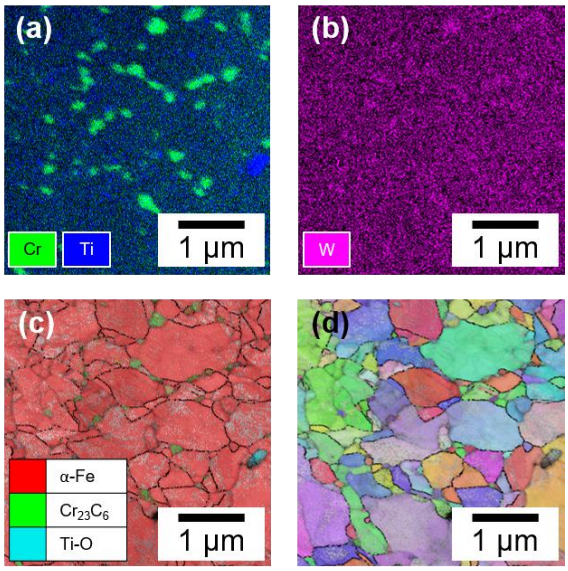

Fig. 10. HE-9Cr specimen showing EDS Cr-Ti map (a) and W map (b), TKD phase map with rather globular $Cr_{23}C_6$ and Ti-O structure identification (c), and TKD orientation map (d).

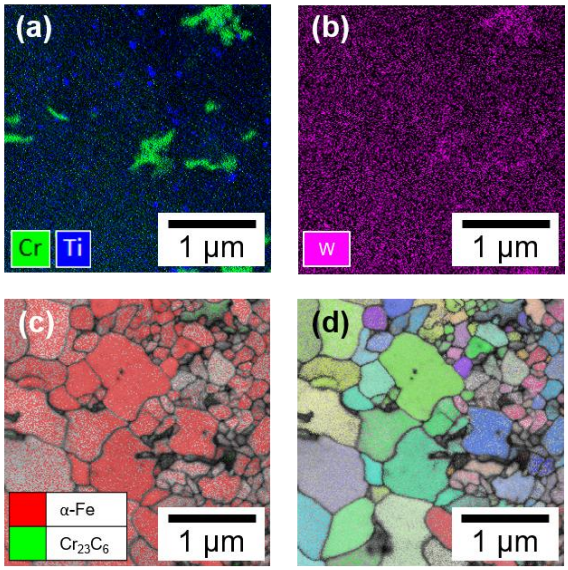

Fig. 11. HIP-9Cr specimen showing EDS Cr-Ti map (a) and W map (b), TKD phase map with grain boundaries shaped $Cr_{23}C_6$ structure identification (c), and TKD orientation map (d).

XRD measurements were performed on the selective dissolution of HE-9Cr-PMill specimen using a laboratory source (Fig. 12) and on HE-9Cr bulk specimen using a synchrotron source (Fig. 13). On the two samples, the $M_{23}C_6$ phases were identified, without any noticeable precipitation of M_7C_3. On the HE-9Cr-PMill the $M_{23}C_6$ composition could be estimated to $(Cr_{14}Fe_8W_1)C_6$ thanks to their high relative volume fraction and the rotating specimen holder suppressing the texture contribution. In the bulk HE-9Cr sample, $M_{23}C_6$ appeared textured, as the intensities calculated from isotropic assumption did not match with the experimental ones, even though Fe and W were introduced into the phase model (Fig. 13). Besides, Ti(C,N) carbides were identified in both specimens with a cell parameter matching again with a high amount of N over C (see **Tab. 3**). A low volume fraction of TiO_2 was also detected on the HE-9Cr specimen. In the selective dissolution specimen (HE-9Cr-PMill), $Y_2Ti_2O_7$ could also be identified, however no Ti-O phases were observed.

The selective dissolution revealed for this grade a total mass fraction of precipitates of approximatively 2.5%. This larger value compared to the Fe-14Cr alloy is consistent with the increment of carbon content, roughly twice larger in the Fe-9Cr than in the Fe-14Cr ODS steels.

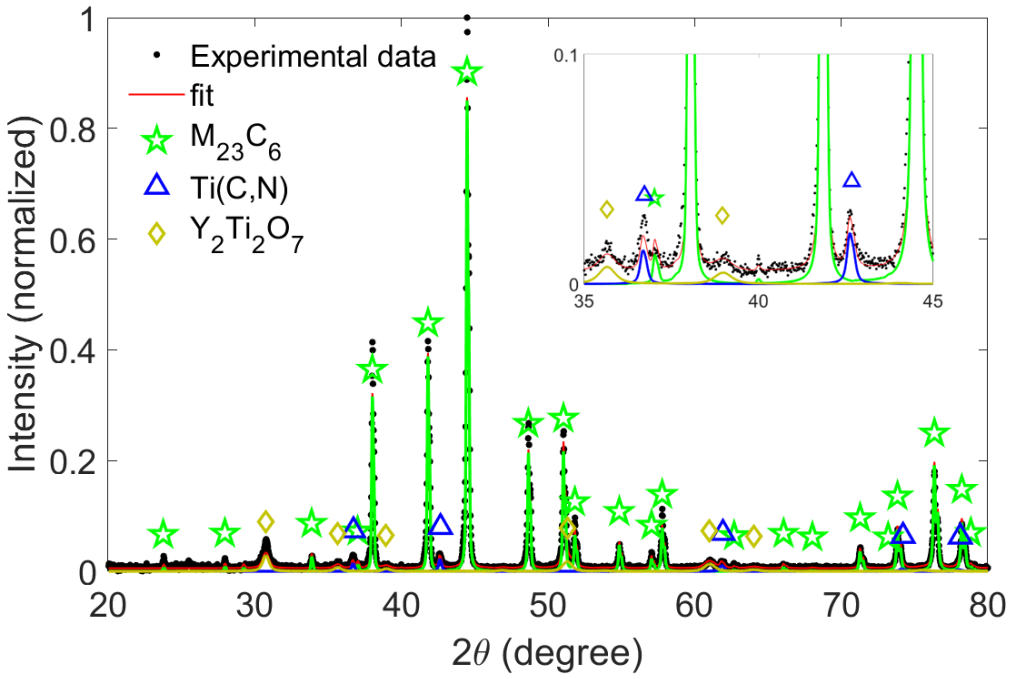

Fig. 12. XRD spectrum of the selective dissolution of HE-9Cr-1 specimen showing $Cr_{23}C_6$ structure, Ti(C,N) and $Y_2Ti_2O_7$ phase identification, showing a magnified view of the region between 35° and 45° of 2θ.

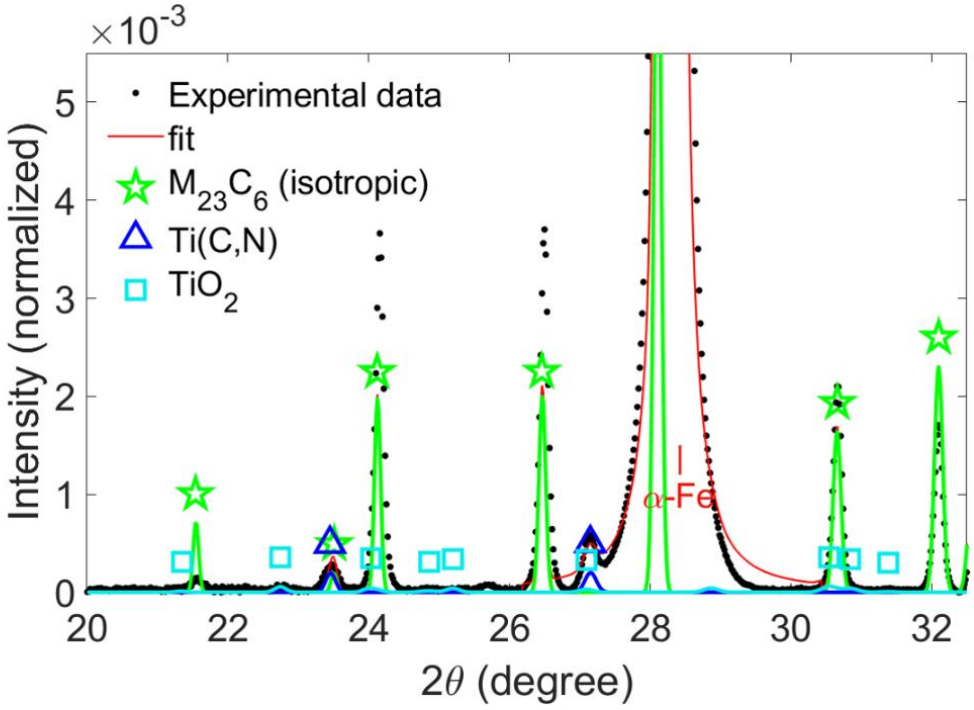

Fig. 13. XRD spectrum of the HE-9Cr-2 specimen showing textured $Cr_{23}C_6$ structure, Ti(C,N) and TiO_2 phase identification.

Tab. 3. Fe-9Cr-1W ODS phases parameters after refinements with estimated errors, reference phases used are completed with space groups and corresponding references.

Phase name	Specimen	Volume fraction	Refined cell parameters (Å)	Phase name
HE-9Cr	$M_{23}C_6$	0.84%	a = 10,600 (±0.001)	$Cr_{23}C_6$ Fm-3m [21]
	Ti(C,N)	0.13%	a = 4.220 (±0.007)	Ti(C,N) Fm-3m [34]
	TiO_2	0.45%	a = 5.223 (±0.014) b = 9.190 (±0.017) c = 5.353 (±0.013)	TiO_2 Pbca [36]
	α-Fe	99.04%	a = 2.865 (neglectable)	α-Fe Im-3m [37]
HE-9Cr-PMill	$M_{23}C_6$	80.1%	a = 10,573 (neglectable)	$Cr_{23}C_6$ Fm-3m [21]
	Ti(C,N)	5.2%	a = 4.239 (neglectable)	Ti(C,N) Fm-3m [34]
	$Y_2Ti_2O_7$	14.6%*	a = 10.068 (±0.002)	$Y_2Ti_2O_7$ Fd-3m [39]

* Relative volume fraction of $Y_2Ti_2O_7$ is probably underestimated as the smaller precipitates were possibly not gathered by the filter.

Phase diagram calculations using Thermocalc software Fe-14Cr, Fe-C have been performed on the Fe-9Cr grades (Fig. 14). As expected, the matrix is fully austenitic above ~850°C. The nature of phases are shown similar to the Fe-14Cr steel (Fig. 7). Ones again Ti(C,N) are present in all regions of the diagrams and is composed by a high amount of N over C. Without suspending the $M_{23}C_6$, the M_7C_3 stability region is extended to lowest value of C content compare with Fe-14Cr. With the oxygen addition $(Ti,Cr)_2O_3$ is the only Ti-O phase predicted by Thermocalc.

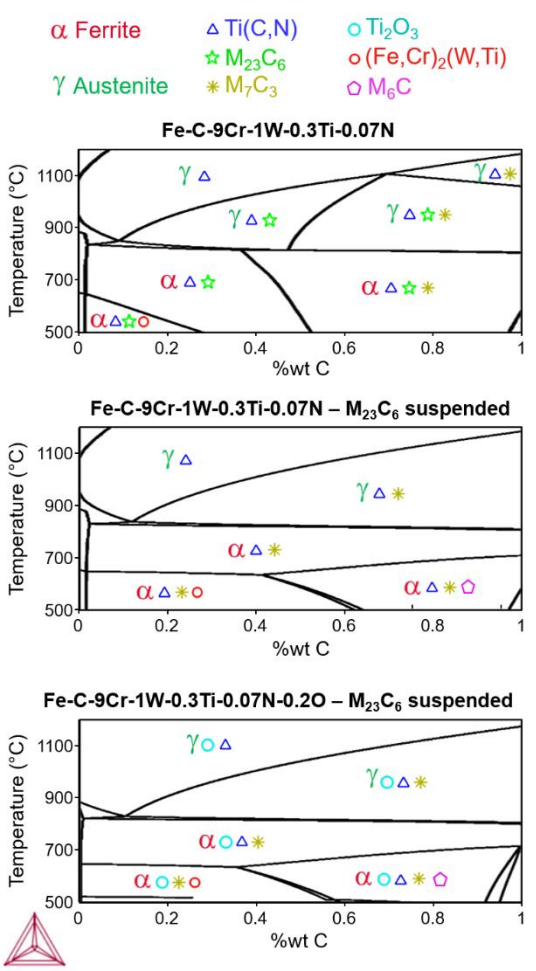

Fig. 14. Simulated phase diagrams of Fe-9Cr-1W-0.3Ti-0.07N(-0.2O) steels computed by Thermocalc software displaying several scenarios with and without $M_{23}C_6$ precipitation.

4. Discussion

The general microstructure of the different ODS grades studied displays common and specific properties mainly related to the fabrication process. The wide grain size observed in every specimens is a common observation in ODS steels where precipitates act as strong pinning points the grain boundaries [40]–[43]. A difference in grain morphology between HE-14Cr and HE-9Cr steels has been observed on each specimen, consistently with previous observations. In each HE-14Cr (Fig. 2c, c' and Fig. 3c, c') the grain shape is columnar, following the extrusion direction and a potential <110> texture parallel to the extrusion direction could be present. This texture information cannot be firmly stated with the available results but is consistent with many studies performed on similar materials and linked to the nano-precipitation preventing recovery and recrystallization [1], [44], [45]. In the HE-9Cr, the phase transformation from ferrite to austenite leads to a renewal of the ferrite grain structure, resulting in equiaxed grains with a more random texture (Fig. 9d, Fig. 10d and Fig. 11d) [18], [46].

Three major points can be stated from the observation of coarse precipitation:

- The nature of the chromium carbides differs from 14Cr grades to 9Cr grades. In 14Cr ODS grades, M_7C_3 together with $M_{23}C_6$ carbides has been identified (Fig. 3, Fig. 4 and Fig. 6) whereas only $M_{23}C_6$ Cr-carbides have been found in each of the 9Cr ODS grades (Fig. 9, Fig. 10, Fig. 11, Fig. 12 and Fig. 13).
- Ti(C,N) precipitates were found in both 14Cr and 9Cr grades. Their cell parameters tends to indicate a predominance of N over C which was confirmed on the HE-14Cr-PMill refinement of the peak intensities resulting in $Ti(C_{0.05},N_{0.95})$ (Fig. 5).
- Ti_2O_3 and/or TiO_2 have also been observed on several grades, but not systematically as shown in the different XRD results (Fig. 5, Fig. 6, Fig. 12 and Fig. 13).
- $Y_2Ti_2O_7$ precipitates were found by XRD on the selective dissolution specimens even if their size are much smaller than the pores of the filter used.

The following table summarizes the different results in terms of coarse precipitation obtained on each of the ODS steels investigated (Tab. 4).

Tab. 4 : Summary of the coarse precipitation results obtained on the 14Cr and 9Cr ODS steels.

Specimens	Precipitates	Observation techniques	Morphologies (seen by TKD/EDS)
HE-14Cr-PMill	$Ti(C_{0.05},N_{0.95})$	TKD+EDS and XRD	Spherical
	Ti_2O_3	EPMA*, XRD	Unknown
	$Y_2Ti_2O_7$	XRD	Unknown
HE-14Cr	M_7C_3	TKD+EDS and XRD	Elongated following GBs
	$M_{23}C_6$	XRD	Unknown
	Ti(C,N)	XRD	Spherical (by EDS observations)
	TiO_2	XRD	Unknown
HIP-14Cr	M_7C_3	TKD+EDS and XRD	Complex shapes following GBs
	$M_{23}C_6$	XRD	Unknown
	Ti(C,N)	XRD	Spherical (by EDS observations)
	TiO_2	XRD	Unknown
HE-9Cr-PMill	$M_{23}C_6$	EPMA*, TKD+EDS and XRD	Following GBs
	Ti(C,N)	XRD	Spherical (by EDS observations)
	$Y_2Ti_2O_7$	XRD	Unknown
HE-9Cr	$M_{23}C_6$	TKD+EDS and XRD	Globular
	Ti(C,N)	XRD	Spherical (by EDS observations)

	TiO_2 / Ti-O	TKD+EDS and XRD	Globular
HIP-9Cr	$M_{23}C_6$	TKD+EDS, XRD	Following GBs
	Ti-rich	EDS	Spherical

* Limit of the spatial resolution of EPMA

At large scale, EPMA results show a Ti and O segregation at PPBs, which could originate from the presence of O at the powder particles surface. Indeed, even if the powder is degassed during the process and milled under high purity argon atmosphere, a residual amount of adsorbed oxygen at the powder surface cannot be excluded. Moreover, as the steel powder contain a high enough amount of chromium (9 to 14 wt%), a chromium oxide passivation layer is very likely to be generated at any contact with the air atmosphere [8], [47]. As a matter of fact, Williams *et al.* demonstrated the formation of Y-Ti-O particles during the milling stage without intentional introduction of oxygen (no introduction of Y_2O_3 powder) [48]. It is therefore not surprising to find O-rich layers at the powder particles boundaries after milling. Oxygen could combine with Ti (also introduced in powder form) as they exhibit a high affinity for each other [49]–[51]. In particular, for Ti-O of large size displayed in the HE-9Cr specimen (Fig. 10c) it cannot be excluded that the TKD maps were acquired on the pathway of a PPB.

According to ThermoCalc calculations, Ti(C,N) carbonitrides are stable in 14Cr or 9Cr ODS grades (containing ~0.05wt%C and ~0.1wt%C respectively) until temperature above 1100°C (Fig. 7). $M_{23}C_6$ carbides are stable until ~900°C for the Fe-14Cr ODS and ~850°C for the Fe-9Cr ODS (Fig. 14). Therefore, the precipitation of $M_{23}C_6$ carbides could occur during the cooling from 1100°C after HE or HIP. Subsequently, the annealing at 1050°C for 1 hour applied on most of HE specimens should dissolve the $M_{23}C_6$ (in part at least) but these phases would precipitate similarly way during the cooling from 1050°C.

However in 14Cr ODS, TKD and XRD measurements indicate the presence of M_7C_3 carbides together with $M_{23}C_6$. The M_7C_3 phases are probably metastable carbides originating from the air-cooling from 1100°C or 1050°C. Similar metastable M_7C_3 had been reported by Wieczerzak *et al.* on a Fe-25Cr-0.79C ferritic steel and attributed to the high cooling rate at solidification (30°C/s) and solid state fast cooling [52]. The same author also showed the enhancement of the M_7C_3 formation over $M_{23}C_6$ during the rapid cooling at the solidification front, attributed to both segregations and lower redistribution of carbides elements [53]. In our alloys, the suspension of $M_{23}C_6$ in Thermocalc calculations leads to a stabilization of M_7C_3 at C low carbon content (very similar to the previous $M_{23}C_6$ stability limit). Moreover, a local enrichment in Cr could stabilize the M_7C_3 over $M_{23}C_6$ as well as a local enrichment in C even though less likely to occur because the diffusion of Cr in Fe [54] is slower than C in Fe [55]. This stabilization of M_7C_3 can even be achieved at almost any C concentration when oxygen is introduced in the simulation with $M_{23}C_6$ suspended, which preferentially combines with Ti rather than with carbon to form $(Ti,Cr)_2O_3$ (Fig. 7).

In the 9Cr ODS steels, only $M_{23}C_6$ carbides were found despite the higher C and lower Cr content as compared to the 14Cr ODS steels, which tends to stabilize M_7C_3 over $M_{23}C_6$ (Fig. 14). An enrichment of $M_{23}C_6$ with W has not been found (and is absent of M_7C_3) which is in good agreement with Inoue *et al.* observations [56] and ThermoCalc calculations. This presence of only $M_{23}C_6$ in the Fe-9Cr materials occurred irrespective of the thermal pathway of the alloys, either after HE/HIP or after annealing at 1050°C for 1h. This difference in terms of Cr-carbides could possibly be explained by the $\gamma \rightarrow \alpha$ phase transformation occurring on the Fe-9Cr grades during cooling which could trigger the transition to the more stable $M_{23}C_6$.

Metastable M_7C_3 precipitates present in Fe-14Cr alloys are very likely to transform into $M_{23}C_6$ at the service temperature, which reaches up to 650°C in a generation IV Sodium-cooled Fast neutron Reactor (SRF). Indeed, Inoue and Matsumoto achieved on a Fe-18.6Cr-3.4W-3.6C (and others) steel the $M_7C_3 \rightarrow M_{23}C_6$ transformation, competed after 10 h at 700°C [56]. Wieczerzak *et al.* observed the transformation $M_7C_3 \rightarrow M_{23}C_6$ from 500 to 600°C by in-situ XRD measurements during a heating ramp on a Fe-24.5Cr-0.79C [52]. This $M_7C_3 \rightarrow M_{23}C_6$ transformation was also reported elsewhere in a 10.5Cr by TEM observation and simulations [57], in a 13Cr steel [58], and the mechanism was determined to be the growth of a $M_{23}C_6$ shell surrounding a M_7C_3 core by experimental observations and thermomechanical simulation [56], [57], [59], [60], [61]. Therefore, in order to trigger the $M_7C_3 \rightarrow M_{23}C_6$ transformation before it could occur in service, a thermal treatment at temperature around 700°C could be applied to Fe-14Cr ODS grades.

The shape of Cr-carbides also varies with the consolidation process. In the HIPed specimens, Cr-carbides are mainly present among the grains of smallest size and exhibit complex shapes and various sizes. HE-14Cr and HE-9Cr-PMill alloys display Cr-carbides following the shapes of the GBs. On the HE-14Cr the columnar grain shape leads to very elongated Cr-carbides. Such elongated shapes of Cr-carbides are likely to increase the anisotropic mechanical behavior of the material [16], [62], already symptomatic of the highly textured columnar grain [63] and could even represent preferential crack initiation sites [64]. In the HE-9Cr material, $M_{23}C_6$ carbides tend to be more globular, which could be explained by the 1050°C-1h annealing which should not be long enough to completely dissolve the $M_{23}C_6$ [17] but would allow the occurrence of a spheroidisation process [16], [52]. These observations are also in favor of performing a thermal treatment below the dissolution temperature of $M_{23}C_6$, at least on HE specimens, in order to remove the detrimental effect of elongated Cr-carbides.

During the lifetime (i.e. several years) and temperature range (i.e. maximum 650°C) of cladding tubes in SFR, Cr-carbides are known to exhibit significant coarsening [65], [66],[57] that could decrease even more the toughness and ductility of the alloy over the time [67], [68]. In particular, as Cr-carbides are intergranular, the coarsening rate of these precipitates can be greatly enhanced by the diffusion along the GBs. Moreover, higher temperature (in accidental

condition or in the range of fusion nuclear power plants) could cause the dissolution of the Cr-carbides and lead to a local Cr and C enrichment of the matrix [23]. Therefore, rather than optimizing the Cr-carbides population by precipitation of stable $M_{23}C_6$ and spheroidization, a straightforward approach would consist in suppressing Cr-carbides in favor of a more stable precipitation.

In every alloy, Ti(C,N) precipitates have been identified (except on HIP-9Cr where Ti(C,N) is only suspected) with a high ratio of N/C content according to their cell parameters. N can be introduced during the milling and subsequent HE step (when HE was applied) [8]. In the HE-14Cr-PMill sample, no Cr-carbides where found, and Ti($C_{0.05}$,$N_{0.95}$) precipitates where identified by XRD and some were also visible on TKD phase maps. The absence of any carbide in HE-14Cr-PMill is surprising as at least few hundred ppm of C is expected from the atomized powder impurities. However, due to the size of the filter pores (220 nm) C-rich Ti(C,N) with small size and volume fraction could be present on the alloy but been removed from the XRD measurements. Nevertheless, absence of Cr-carbide certainly due to the lower carbon contamination of the steel, highlights that an optimization of the carbides precipitation can be achieved by controlling the impurities addition at the milling step.

Ti(C,N) displays a fine precipitation and should be resistant to coarsening at high temperatures and therefore should not be detrimental to the alloy strength. However, their potential contribution in improving the yield strength in a similar way as in similar non-ODS steel grades [69] is unclear as a high strength already arises from the extremely fine and dense Y-Ti-O nano-oxides of ODS alloys.

It is interesting to notice that no C-rich Ti(C,N) were identified in any of our ODS grades. As Ti(C,N) is the only carbon containing phase stable above 800 - 900°C (Fig. 7 and Fig. 14), a thermal treatment above this temperature should enhance their formation over Cr-carbides. Indeed, Zhao *et al.* succeeded to completely suppress the $M_{23}C_6$ precipitation with a thermal treatment of 1200°C for 5 h [17]. The heat treatment for one hour at 1050°C applied in the present study did not demonstrate any efficiency to precipitate, C-rich Ti(C,N) possibly because the holding time or temperature were not sufficient or because the amount of Ti was available in solid solution is not sufficient. Ti(C,N) precipitation is generally thinner, well dispersed and more resistant to thermal coarsening than $M_{23}C_6$ [17], [69]. Thus, inducing the precipitation of C-rich Ti(C,N) at the expense of Cr-carbides would allow to get rid of the drawbacks involved by the Cr-carbides population presence mentioned previously, particularly the harmful evolution of the mechanical properties during thermal aging. Thus, further investigations on the effect a thermal treatment performed at different temperatures and holding times would be of great interest. Such experiments would require careful microstructural characterizations as at the high temperature required (i.e. in the range of 1200°C) existing Ti(C,N) precipitates, grain

size and/or morphologies or even nano-oxide precipitation size (especially for the Fe-9Cr alloys [70], [71]) could also evolve significantly.

So far, the presence of TiO_2 or Ti_2O_3 in ODS steels is still poorly understood and has been shown to be elusive as no Ti oxides were observed in the HE-9Cr-PMill specimen. EPMA results demonstrate that Ti-oxides location at the PPB is highly probable, especially in Fe-14Cr specimens. It can be noted that Ti-O formation should be preferential over Ti(C,N) accordingly to their respective formation enthalpies [72], [73]. However, the precipitation of Ti-O phases are driven by the amount of oxygen available in solid solution, which should be already consumed by the formation of Y-Ti-O nano-precipitates, the most stable oxide phase. The precipitation of Ti-O seems therefore to be linked with several intricated factors: Ti(C,N), Y-Ti-O precipitation and the local availability of oxygen in solid solution, particularly at the vicinity of the PPB where it may be higher, which make the understanding of their formation mechanism difficult. A summary of the different features observed in this study as well as the different chemical competition between the precipitates and rough estimates of their sizes are given in the Fig. 15.

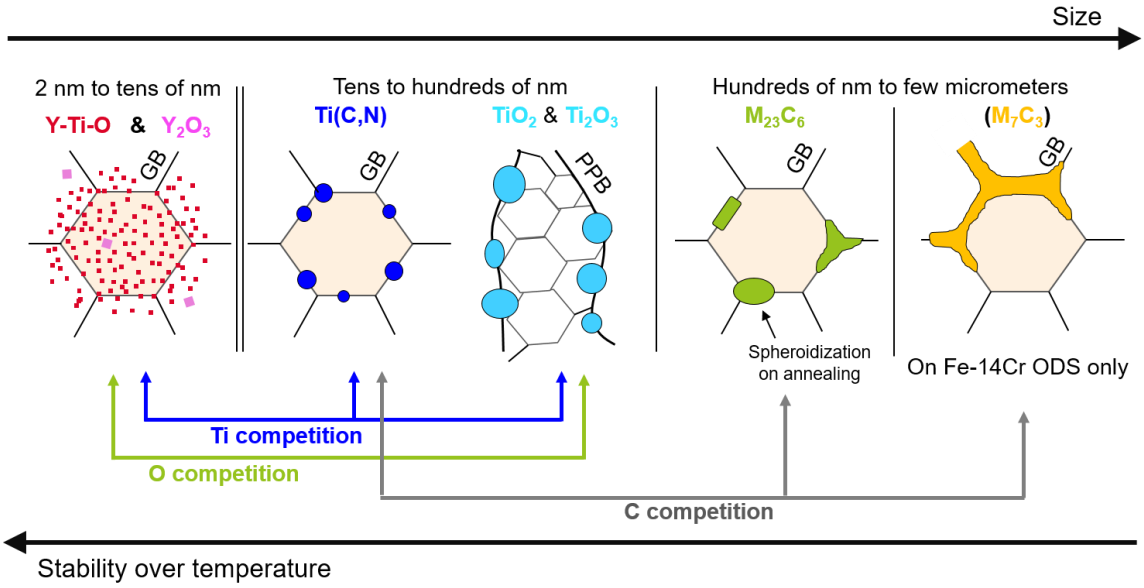

Fig. 15. Scheme showing the nano-oxides and different coarse precipitates encountered in this study, showing their morphologies as well as a rough estimate of their size.

5. Conclusions

Several ODS steels have been observed by means of EPMA, TKD and XRD measurements. Cr-carbides, Ti-carbonitrides and Ti-oxides have been found and present different characteristics depending on the ODS grades.

In purely ferritic steels (Fe-14Cr), both Cr-rich $M_{23}C_6$ and metastable M_7C_3 carbides have been found whereas ferritic / martensitic (Fe-9Cr) steels show only Cr-rich $M_{23}C_6$ carbides also

enriched in W. This difference in Cr-carbides nature could be linked to the austenite-ferrite phase transformation. The presence of metastable precipitates are not suitable for industrial use as they are likely to transform at the working temperature of sodium cooled fast reactors into $M_{23}C_6$, changing the mechanical behavior of the material in an unknown way.

In Fe-14Cr HE alloys, Cr-carbides exhibit elongated shapes that could increase the anisotropy of the material and represent preferential sites of fracture initiation.

The application of a thermal treatment after elaboration at temperature close to 700°C for few hours could induce a spheroidisation of Cr-carbides (as shown on the HE-9Cr specimen) and the $M_7C_3 \rightarrow M_{23}C_6$ transformation before the introduction of the cladding to the SFR. In HIP specimens, Cr-carbides exhibit complex shapes and tend to be located among the small grains of the bimodal distribution. In all cases, Cr-carbides were found to be intergranular.

Besides, all ODS grades display Ti-rich globular precipitates. Ti(C,N) displaying high amount of N over C has been identified in all samples except in the HIP-9Cr where Ti(C,N) were not clearly identified but suspected. Ti oxides were also found, particularly in the PPB, where a higher than average composition in oxygen is presumed after milling (as-MA state). The location of Ti-rich precipitates is ambiguous as few have been identified by TKD. Yet, these precipitates also seem to be mainly located at GBs.

6. Acknowledgment

The authors acknowledge Jean-Christophe Brachet for his help and fruitful discussion on the precipitation analysis and Francoise Barcelo for her precious help on TKD measurements acquisition.

7. References

[1] S. Ukai, S. Ohtsuka, T. Kaito, Y. de Carlan, J. Ribis, J. Malaplate, Oxide dispersion-strengthened/ ferrite-martensite steels as core materials for Generation IV nuclear reactors, Structural Materials for Generation IV Nuclear Reactors. 10 (2017) 357-414, doi: 10.1016/B978-0-08-100906-2.00010-0.

[2] S.J. Zinkle, J.L. Boutard, D.T. Hoelzer, A. Kimura, R. Lindau, G.R. Odette, M. Rieth, L. Tan, H. Tanigawa, Development of next generation tempered and ODS reduced activation ferritic/martensitic steels for fusion energy applications, Nucl. Fusion. 57 (9) (2017) 92005, doi: 10.1088/1741-4326/57/9/092005.

[3] J.L. Boutard, V. Badjeck, L. Barguet, C. Barouh, A. Bhattacharya, Y. Colignon, C. Hatzoglou, M. Loyer-Prost, A.L. Rouffié, N. Sallez, H. Salmon-Legagneur, T. Schuler, Oxide dispersion strengthened ferritic steels: a basic research joint program in France, J. Nucl. Mater. 455 (1–3) (2014) 605–611, doi: 10.1016/j.jnucmat.2014.08.059.

[4] N. Oono, S. Ukai, Precipitation of Oxide Particles in Oxide Dispersion Strengthened (ODS) Ferritic Steels, Mater. Trans. 59 (10) (2018) 1651–1658, doi: 10.2320/matertrans.M2018110.

[5] M.K. Miller, C.M. Parish, Q. Li, Advanced oxide dispersion strengthened and nanostructured ferritic alloys, Mater. Sci. Technol. 29 (10) (2013) 1174–1178, doi: 10.1179/1743284713Y.0000000207.

[6] P. He, M. Klimenkov, R. Lindau, A. Möslang, Characterization of precipitates in nano structured 14% Cr ODS alloys for fusion application, J. Nucl. Mater. 428 (1–3) (2012) 131–138, doi: 10.1016/j.jnucmat.2011.08.026.

[7] H. Sakasegawa, L. Chaffron, F. Legendre, L. Boulanger, T. Cozzika, M. Brocq, Y. de Carlan, Correlation between chemical composition and size of very small oxide particles in the MA957 ODS ferritic alloy, J. Nucl. Mater. 384 (2) (2009) 115–118, doi: 10.1016/j.jnucmat.2008.11.001.

[8] P. Olier, M. Couvrat, C. Cayron, N. Lochet, L. Chaffron, Incidence of mechanical alloying contamination on oxides and carbides formation in ODS ferritic steels, J. Nucl. Mater. 442 (1–3) (2013) S106–S111, doi: 10.1016/j.jnucmat.2013.03.090.

[9] Z. Oksiuta, P. Olier, Y. de Carlan, N. Baluc, Development and characterisation of a new ODS ferritic steel for fusion reactor application, J. Nucl. Mater. 393 (1) (2009) 114–119, doi: 10.1016/j.jnucmat.2009.05.013.

[10] A. Chauhan, D. Litvinov, Y. de Carlan, J. Aktaa, Study of the deformation and damage mechanisms of a 9Cr-ODS steel: Microstructure evolution and fracture characteristics, Mater. Sci. Eng. A, 658 (2016) 123–134, doi: 10.1016/j.msea.2016.01.109.

[11] L. Straßberger, D. Litvinov, J. Aktaa, High temperature tensile properties of oxide dispersion strengthened T91 and their correlation with microstructural evolution, Mater. Sci. Technol. 30 (13) (2014) 1691–1696, doi: 10.1179/1743284714Y.0000000562.

[12] V. de Castro, T. Leguey, M.A. Auger, S. Lozano-Perez, M.L. Jenkins, Analytical characterization of secondary phases and void distributions in an ultrafine-grained ODS

Fe–14Cr model alloy, J. Nucl. Mater. 417 (2011) (1–3) 217–220, doi: 10.1016/j.jnucmat.2010.12.067.

[13] F. Abe, Precipitate design for creep strengthening of 9% Cr tempered martensitic steel for ultra-supercritical power plants, Sci. Technol. Adv. Mater. 9 (1) (2008) 013002, doi: 10.1088/1468-6996/9/1/013002.

[14] M.J. Alinger, G.R. Odette, D.T. Hoelzer, The development and stability of Y-Ti-O nanoclusters in mechanically alloyed Fe-Cr based ferritic alloys, J. Nucl. Mater. 329–333 (2004) 382–386, doi: 10.1016/j.jnucmat.2004.04.042.

[15] J. Ribis, M.L. Lescoat, S.Y. Zhong, M.H. Mathon, Y. de Carlan, Influence of the low interfacial density energy on the coarsening resistivity of the nano-oxide particles in Ti-added ODS material, J. Nucl. Mater. 442 (1–3) (2013) S101–S105, doi: 10.1016/j.jnucmat.2012.10.051.

[16] M. Klimiankou, R. Lindau, A. Möslang, "Direct correlation between morphology of (Fe,Cr)23C6 precipitates and impact behavior of ODS steels," J. Nucl. Mater. vol. 367–370, pp. 173–178, Aug. 2007, doi: 10.1016/j.jnucmat.2007.03.150.

[17] Q. Zhao, Z. Ma, L. Yu, H. Li, C. Liu, C. Li, Y. Liu, Tailoring the secondary phases and mechanical properties of ODS steel by heat treatment, J. Mater. Sci. Technol. 35 (6) (2019) 1064–1073, doi: 10.1016/j.jmst.2018.12.008.

[18] L. Toualbi, C. Cayron, P. Olier, J. Malaplate, M. Praud, M.H. Mathon, D. Bossu, E. Rouesne, A. Montani, R. Logé, Y. de Carlan, Assessment of a new fabrication route for Fe-9Cr-1W ODS cladding tubes, J. Nucl. Mater. 428 (1–3) (2012) 47–53, doi: 10.1016/j.jnucmat.2011.12.013.

[19] S. Ukai, S. Mizuta, M. Fujiwara, T. Okuda, T. Kobayashi, Development of 9Cr-ODS Martensitic Steel Claddings for Fuel Pins by means of Ferrite to Austenite Phase Transformation, J. Nucl. Sci. Technol. 39 (7) (2002) 778–788, doi: 10.1080/18811248.2002.9715260.

[20] H.R.Z. Sandim, R.A. Renzetti, A.F. Padilha, D. Raabe, M. Klimenkov, R. Lindau, A. Möslang, Annealing behavior of ferritic-martensitic 9%Cr-ODS-Eurofer steel, Mater. Sci. Eng. A. 527 (15) (2010) 3602–3608, doi: 10.1016/j.msea.2010.02.051.

[21] A. L. Bowman, G. P. Arnold, E. K. Storms and N. G. Nereson, The crystal structure of Cr23C6, Acta Crystallogr. B. 28 (1972) 3102-3103, doi: 10.1107/S0567740872007526.

[22] P. Parameswaran, M. Vijayalakshmi, P. Shankar, V. S. Raghunathan, Influence of carbon content on microstructure and tempering behaviour of 2 1/4 Cr 1 Mo steel, J. Mater. Sci. 28 (20) (1993) 5426–5434, doi: 10.1007/BF00367811.

[23] N. Dudova, R. Kaibyshev, On the Precipitation Sequence in a 10%Cr Steel under Tempering, ISIJ Int. 51 (5) (2011) 826–831, doi: 10.2355/isijinternational.51.826.

[24] B. Sitaud, P.L. Solari, S. Schlutig, I. Llorens, H. Hermange (2012) Characterization of radioactive materials using the MARS beamline at the synchrotron SOLEIL, J. Nucl. Mater. 425 (1–3) 238–24, doi:10.1016/j.jnucmat.2011.08.017.

[25] L. Lutterotti, Total pattern fitting for the combined size–strain–stress–texture determination in thin film diffraction, Nucl. Instrum. Methods Phys. Res. Sect. B. 268 (3–4) (2010) 334–340, doi: 10.1016/j.nimb.2009.09.053.

[26] L. Lutterotti, M. Bortolotti, G. Ischia, I. Lonardelli, H.R. Wenk, Rietveld texture analysis from diffraction images, Z. Für Krist. Suppl. 26 (2007) 125–130, doi: 10.1524/zksu.2007.2007.suppl_26.125.

[27] T.H. de Keijser, J.I. Langford, E.J. Mittemeijer, A.B.P. Vogels, Use of the Voigt function in a single-line method for the analysis of X-ray diffraction line broadening, J. Appl. Crystallogr. 15 (3) (1982) 308–314, doi: 10.1107/S0021889882012035.

[28] A. Le Bail, Whole powder pattern decomposition methods and applications: A retrospection, Powder Diffr. 20 (4) (2005) 316–326, doi: 10.1154/1.2135315.

[29] J.O. Andersson, T. Helander, L. Höglund, P. Shi, B. Sundman, Thermo-Calc & DICTRA, computational tools for materials science, Calphad. 26 (2) (2002) 273–312, doi: 10.1016/S0364-5916(02)00037-8.

[30] M. Dadé, J. Malaplate, J.C. Brachet, T. Guilbert, C. Toffolon-Masclet, Influence of chemical composition on the microstructure and phase transformations of Fe-14Cr ferritic steels, Materialia. 7 (2019) 100388, doi: 10.1016/j.mtla.2019.100388.

[31] D. Sornin, P.F. Giroux, E. Rigal, D. Fabregue, R. Soulas, D. Hamon, Influence of Powder Outgassing Conditions on the Chemical, Microstructural, and Mechanical Properties of a 14 wt% Cr Ferritic ODS Steel, Metall. Mater. Trans. A. 48 (11) (2017) 5559–5566, doi: 10.1007/s11661-017-4320-6.

[32] X. Boulnat, D. Fabrègue, M. Perez, S. Urvoy, D. Hamon, Y. de Carlan, Assessment of consolidation of oxide dispersion strengthened ferritic steels by spark plasma sintering: from laboratory scale to industrial products, Powder Metall. 57 (3) (2014) 204–211, doi: 10.1179/1743290114Y.0000000091.

[33] M. Dadé, J. Malaplate, J. Garnier, F. De Geuser, F. Barcelo, P. Wident, A. Deschamps, Influence of microstructural parameters on the mechanical properties of oxide dispersion strengthened Fe-14Cr steels, Acta Mater. 127 (2017) 165–177, doi: 10.1016/j.actamat.2017.01.026.

[34]: B. Jiang, N. Ying, Q. Wang, J. Xiao, K. Huang, J. Hou, H. Zhu, Structural and Thermodynamics Properties of $TiC_{1-x}N_x$–$TiO_{1-x}N_x$ Solid Solutions: X-ray Diffraction and First-Principles Approaches, J. Am. Ceram. Soc. 97 (2014) 1288-1295, doi: 10.1111/jace.12761

[35]: F. McClune, New X-Ray Powder Diffraction Patterns from the JCPDS Associateship, Powder Diffr. 1 (1986) 77-99, doi: 10.1017/S0885715600011337.

[36]: E. Silva Junior, F.A. La Porta, M.S. Liu, J. Andrés, J.A. Varela, E. Longo, A relationship between structural and electronic order–disorder effects and optical properties in

crystalline TiO2 nanomaterial, Dalton Trans. 44 (2015) 3159-3175, doi: 10.1039/C4DT03254C.

[37]: A.W. Hull, A New Method of X-Ray Crystal Analysis, Phys. Rev. 10 (1917) 661, doi: 10.1103/PhysRev.10.661.

[38]: S.C. Abrahams, Magnetic and Crystal Structure of Titanium Sesquioxide, Phys. Rev. 130 (1963) 2230, doi: 10.1103/PhysRev.130.2230.

[39]: G.J. Li, L.M. Xu, C. Fan, F.B. Zhang, Y.Y. Lv, B. Ni, Z.Y. Zhao, X.F. Sun, Single crystal growth of the pyrochlores $R_2Ti_2O_7$ (R=rare earth) by the optical floating-zone method J. Cryst. Growth. 377 (2013) 96-100, doi: 10.1016/j.jcrysgro.2013.04.048.

[40] X. Boulnat, N. Sallez, M. Dadé, A. Borbély, J.L. Béchade, Y. de Carlan, J. Malaplate, Y. Bréchet, F. De Geuser, A. Deschamps, P. Donnadieu, D. Fabrègue, M. Perez, Influence of oxide volume fraction on abnormal growth of nanostructured ferritic steels during non-isothermal treatments: An in situ study, Acta Mater. 97 (2015) 124–130, doi: 10.1016/j.actamat.2015.07.005.

[41] H. Zhang, Y. Huang, H. Ning, C.A. Williams, A.J. London, K. Dawson, Z. Hong, M.J. Gorley, C.R.M. Grovenor, G.J. Tatlock, S.G. Roberts, M.J. Reece, H. Yan, P.S. Grant, Processing and microstructure characterisation of oxide dispersion strengthened Fe-14Cr-0.4Ti-0.25Y2O3 ferritic steels fabricated by spark plasma sintering, J. Nucl. Mater. 464 (2015) 61–68.

[42] C.C. Eiselt, M. Klimenkov, R. Lindau, A. Möslang, H.R.Z. Sandim, A.F. Padilha, D. Raabe, High-resolution transmission electron microscopy and electron backscatter diffraction in nanoscaled ferritic and ferritic-martensitic oxide dispersion strengthened-steels, J. Nucl. Mater. 385 (2009) 231–235, doi: 10.1016/j.jnucmat.2008.11.029.

[43] J.H. Kim, C.H. Park, Effect of milling temperature on nanoclusters and ultra fine grained microstructure of oxide dispersion strengthened steel, J. Alloys Compd. 585 (2014) 69–74, doi: 10.1016/j.jallcom.2013.09.085.

[44] J. Hoffmann, M. Rieth, L. Commin, S. Antusch, Microstructural anisotropy of ferritic ODS alloys after different production routes, Fusion Eng. Des. 98–99 (2015) 1986–1990, doi: 10.1016/j.fusengdes.2015.05.002.

[45] Z. Oksiuta, P. Hosemann, S. C. Vogel, N. Baluc, Microstructure examination of Fe–14Cr ODS ferritic steels produced through different processing routes, J. Nucl. Mater. 451 (1–3) (2014) 320–327, doi: 10.1016/j.jnucmat.2014.04.004.

[46] E. Vakhitova, D. Sornin, F. Barcelo, M. François, Texture evolution in Oxide Dispersion Strengthened (ODS) steel tubes during pilgering process, J. Nucl. Mater. 494 (2017) 20–28, doi: 10.1016/j.jnucmat.2017.07.002.

[47] H. Hadraba, R. Husak, L. Stratil, F. Siska, Z. Chlup, V. Puchy, J. Michalicka, Survey of oxide candidate for advanced 9%, 14% and 17%Cr ODS steels for fusion applications, Fusion Eng. Des. 124 (2017) 1028–1032, doi: 10.1016/j.fusengdes.2017.04.048.

[48] C.A. Williams, P. Unifantowicz, N. Baluc, G.D.W. Smith, E.A. Marquis, The formation and evolution of oxide particles in oxide-dispersion-strengthened ferritic steels during processing, Acta Mater. 61 (6) (2013) 2219–2235, doi: 10.1016/j.actamat.2012.12.042.

[49] C.L. Fu, M. Krčmar, G.S. Painter, X.Q. Chen, Vacancy mechanism of high oxygen solubility and nucleation of stable oxygen-enriched clusters in Fe, Phys. Rev. Lett. 99 (2007) 1–4, doi: 10.1103/PhysRevLett.99.225502.

[50] M.K. Miller, C.L. Fu, M. Krcmar, D.T. Hoelzer, C. T. Liu, Vacancies as a constitutive element for the design of nanocluster-strengthened ferritic steels, Front. Mater. Sci. China. 3 (2009) 9–14, doi: 10.1007/s11706-009-0001-8.

[51] A. Claisse, P. Olsson, First-principles calculations of (Y, Ti, O) cluster formation in body centred cubic iron-chromium, Nucl. Instrum. Methods Phys. Res. Sect. B Beam Interact. Mater. At., 303 (2013) 18–22, doi: 10.1016/j.nimb.2013.01.016.

[52] K. Wieczerzak, P. Bala, R. Dziurka, T. Tokarski, G. Cios, T. Koziel, L. Gondek, The effect of temperature on the evolution of eutectic carbides and $M_7C_3 \rightarrow M_{23}C_6$ carbides reaction in the rapidly solidified Fe-Cr-C alloy, J. Alloys Compd. 698 (2017) 673–684, doi: 10.1016/j.jallcom.2016.12.252.

[53] K. Wieczerzak, P. Bala, M. Stepien, G. Cios, T. Koziel, Formation of eutectic carbides in Fe–Cr–Mo–C alloy during non-equilibrium crystallization, Mater. Des. 94 (2016) 61–68, doi: 10.1016/j.matdes.2016.01.028.

[54] R. Braun, M. Feller-Kniepmeier, Diffusion of Chromium in α-Iron, phys. stat. sol. (a). 90 (2) (1985) 553–561, doi: 10.1002/pssa.2210900219.

[55] C.A. Wert, Diffusion Coefficient of C in α-Iron, Phys. Rev. 79 (1950) 601–605, doi: 10.1103/PhysRev.79.601.

[56] A. Inoue, T. Masumoto, Carbide reactions (M3C→M7C3→M23C6→M6C) during tempering of rapidly solidified high carbon Cr-W and Cr-Mo steels, Metall. Trans. A. 11 (5) (1980) 739–747, doi: 10.1007/BF02661203.

[57] A. Bjärbo, M. Hättestrand, Complex carbide growth, dissolution, and coarsening in a modified 12 pct chromium steel—an experimental and theoretical study, Metall. and Mat. Trans. A. 32 (2001) 19–27, doi: 10.1007/s11661-001-0247-y.

[58] M. Wang, Z. Zhou, L. Wu, Y. Ding, Z. Wang, Characterization and in-situ formation mechanism of tungsten carbide reinforced Fe-based alloy coating by plasma cladding, Int. J. Miner. Metall. Mater. 25 (4) (2018) 439–443, doi: 10.1007/s12613-018-1589-4.

[59] A. Wiengmoon, Carbides in High Chromium Cast Irons, Naresuan Univ. Eng. J. 6 (2011) 64–70, doi: https://doi.org/10.14456/nuej.2011.6.

[60] M. Wang, D. Flahaut, Z. Zhang, I.P. Jones, Y.L. Chiu, Primary carbide transformation in a high performance micro-alloy at 1000 °C, J. Alloys Compd. 781 (2019) 751–760, doi: 10.1016/j.jallcom.2018.12.095.

[61] K. Wang, D. Li, Formation of core (M_7C_3)-shell ($M_{23}C_6$) structured carbides in white cast irons: A thermo-kinetic analysis, Comput. Mater. Sci. 154 (2018) 111–121, doi: 10.1016/j.commatsci.2018.07.032.

[62] M. Klimenkov, R. Lindau, U. Jäntsch, A. Möslang, Effect of irradiation temperature on microstructure of ferritic-martensitic ODS steel, J. Nucl. Mater. 493 (2017) 426–435, doi: 10.1016/j.jnucmat.2017.06.024.

[63] M. Serrano, M. Hernández-Mayoral, A. García-Junceda, Microstructural anisotropy effect on the mechanical properties of a 14Cr ODS steel, J. Nucl. Mater. 428 (1–3) (2012) 103–109, doi: 10.1016/j.jnucmat.2011.08.016.

[64] L. Zheng, X. Hu, X. Kang, D. Li, Precipitation of $M_{23}C_6$ and its effect on tensile properties of 0.3C–20Cr–11Mn–1Mo–0.35N steel, Mater. Des. 78 (2015) 42–50, doi: 10.1016/j.matdes.2015.04.016.

[65] Y. Xu, X. Zhang, Y. Tian, C. Chen, Y. Nan, H. He, M. Wang, Study on the nucleation and growth of $M_{23}C_6$ carbides in a 10% Cr martensite ferritic steel after long-term aging," Mater. Charact. 111 (2016) 122–127, doi: 10.1016/j.matchar.2015.11.023.

[66] X. Hu, L. Li, X. Wu, M. Zhang, Coarsening behavior of $M_{23}C_6$ carbides after ageing or thermal fatigue in AISI H13 steel with niobium, Int. J. Fatigue. 28 (3) (2006) 175–182, doi: 10.1016/j.ijfatigue.2005.06.042.

[67] A. Grybėnas, V. Makarevičius, A. Baltušnikas, I. Lukošiūtė, R. Kriūkienė, Correlation between structural changes of $M_{23}C_6$ carbide and mechanical behaviour of P91 steel after thermal aging, Mater. Sci. Eng. A. 696 (2017) 453–460, doi: 10.1016/j.msea.2017.04.103.

[68] J. Li, C. Zhang, B. Jiang, L. Zhou, Y. Liu, Effect of large-size $M_{23}C_6$-type carbides on the low-temperature toughness of martensitic heat-resistant steels, J. Alloys Compd. 685 (2016) 248–257, doi: 10.1016/j.jallcom.2016.05.294.

[69] W. Saikaly, X. Bano, C. Issartel, G. Rigaut, L. Charrin, A. Charai, The Effects of Thermomechanical Processing on the Precipitation in an Industrial Dual-Phase Steel Microalloyed with Titanium, Metall. and Mat. Trans. A. 32 (2001) 1939–1947 doi: 10.1007/s11661-001-0006-0.

[70] M. Yamamoto, S. Ukai, S. Hayashi, T. Kaito, S. Ohtsuka, Reverse phase transformation from α to γ in 9Cr-ODS ferritic steels, J. Nucl. Mater. 417 (1-3) (2011) 237–240, doi: 10.1016/j.jnucmat.2010.12.250.

[71] S.W. Kim, T. Shobu, S. Ohtsuka, T. Kaito, M. Inoue, M. Ohnuma, Kinetic Approach for Growth and Coalescence of Nano-Size Oxide Particles in 9Cr-ODS Steel Using High-Energy Synchrotron Radiation X-rays in SPring-8, Mater. Trans. 50 (4) (2009) 917–921, doi: 10.2320/matertrans.MER2008439

[72]: G.L. Humphrey, The Heats of Combustion and Formation of Titanium Nitride (TiN) and Titanium Carbide (TiC), Journal of the American Chemical Society. 73 (5) (1951) 2261-2263, doi: 10.1021/ja01149a100.

[73]: T.V. Charlu, O.J. Kleppa, T.B. Reed, High-temperature combustion calorimetry III. Enthalpies of formation of titanium oxides, The Journal of Chemical Thermodynamics. 6 (11) (1974) 1065-1074, doi: 10.1016/0021-9614(74)90068-8.